ELSEVIER

Contents lists available at ScienceDirect

Colloids and Surfaces A

journal homepage: www.elsevier.com/locate/colsurfa



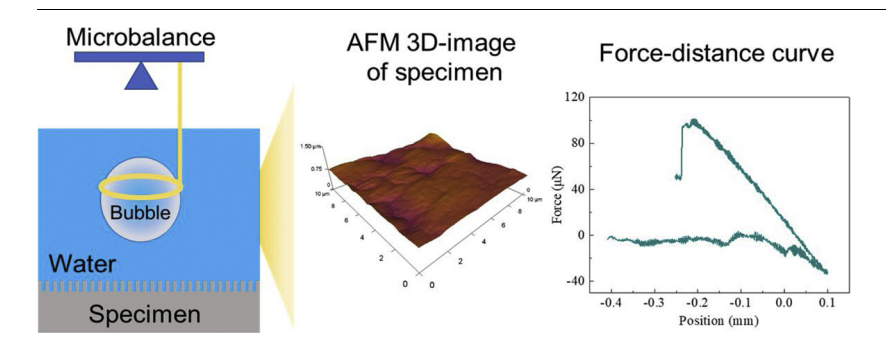
Nano-scaled roughness effect on air bubble-hydrophilic surface adhesive strength



Donghui Wang^{a,b}, Zhanglei Zhu^{a,b}, Bin Yang^a, Wanzhong Yin^{a,c,**}, Jaroslaw W. Drelich^{b,*}

- ^a School of Resources and Civil Engineering, Northeastern University, Shenyang, 110819, China
- b Department of Materials Science and Engineering, Michigan Technological University, Houghton, 49931, United States
- ^c Genetic Mineral Processing Research Center, Northeastern University, Shenyang, 110819, China

GRAPHICAL ABSTRACT



$A\;R\;T\;I\;C\;L\;E\;\;I\;N\;F\;O$

Keywords: Adhesion force Contact angle Roughness Wettability

ABSTRACT

Surface roughness of solid affects its interactions with gas bubbles in water. Here, we investigate the effect of surface nano-scaled (random) roughness, quantified with the root-mean-square (RMS) roughness from about 3 to 260 nm, on the adhesive strength of air bubble with natural hydrophilic hematite and pyrite surfaces using a microelectronic balance-camera system. The recorded values include bubble-mineral adhesion forces, water contact angles, and bubble base diameters during stages of air bubble attachment and spreading, maximum adhesion, and detachment. The results confirm weakening of adhesive forces for air bubble with hydrophilic surfaces of increasing nano-scale roughness. The study reveals a linear dependency between adhesion force and RMS roughness. The adhesion force was also found to be in a linear correlation with contact angle and its sine function, providing evidence for the surface tension force dominance in adhesion of bubble to hydrophilic surface with nano-scaled surface roughness characteristics of random nature.

1. Introduction

Interactions of gas bubbles with solid surfaces play a pivotal role in many industrial applications. For example, through the use of froth flotation, gas bubbles have been used for decades in a selective separation and purification of particulates including processing of mineral ores [1–3], deinking of wastepaper [4,5], plastics recycling [6–8], wastewater treatments [9,10], bitumen extraction [11–14], and coal upgrading [15,16]. Many food products [17–21] and cosmetics [22–25] are formulated through engineering of bubbles into structured foams

^{*} Corresponding author.

^{**} Corresponding author at School of Resources and Civil Engineering, Northeastern University, Shenyang, 110819, China. E-mail addresses: yinwanzhong@mail.neu.edu.cn (W. Yin), jwdrelic@mtu.edu (J.W. Drelich).

stabilized with fine particles. Bubbles also attract interest in designing a new generation of microfluidic devices for transport of materials or even to perform logical control operations [26,27]. Bubble-driven micropumps have shown the potential to reduce fabrication cost and improve reliability and could be used in microanalytical systems, microelectronic cooling systems, drug delivery applications, and chemical-reactors [28–34]. Therefore, understanding the bubble-solid surface interactions and factors that control them is not only of fundamental scientific interest, it has implications into designing more efficient industrial operations and technologies.

Mainly through fundamental research on froth flotation of minerals. it is now well documented that interactions between gas bubbles and solids are governed by chemical and physical characteristics of interacting surfaces, combined with composition and physical properties of liquid surrounding gas and solid phases [35-44]. One factor that received more attention in recent years is surface roughness of floated particles as recording of changes in flotation recovery and kinetics is not complicated and most of the time reproducible [45,46]. With new and improved imaging characterization tools, it is now often possible to link nano-scaled surface roughness with its effect on interactions with particulates including gas bubbles. Indeed, our most recent report demonstrates a positive effect of surface nano-scaled surface roughness on flotation recovery of (hydrophilic) magnesite particles [46]. Theoretical analysis of colloidal forces suggests that the nano-sized asperities reduce energy barrier during interactions of gas bubbles with solid surfaces [45-47]. It remains, however, unexplored whether any other factors in bubble-surface interactions are affected by nano-sized asperities.

Here, two hydrophilic natural specimens, hematite (Fe2O3) and pyrite (FeS2) were selected, both having different chemistry but similar affinity to water in term of contact angle (66 \pm 3° vs. 58 \pm 2° for hematite and pyrite, respectively). Both specimens were polished through multi-stage protocol to produce fresh surfaces of varying nanoscaled roughness characteristics (RMS = 3-260 nm), imaged and quantified using atomic force microscopy (AFM). Then, the measurements of interacting forces between air bubble and mineral surface were carried out in water using a microbalance during bubble attachment, spreading, adhesion, and detachment. The results confirm enhanced interactions of hydrophilic minerals having increasing nanoscaled surface roughness with water at the expense of interactions with air bubble. A linear dependence of adhesion force with root-meansquare (RMS) roughness is reported for both minerals. Also, the experimental adhesion forces depend linearly on contact angle and its sine function, suggesting that the three-phase contact line follows closely the roughness profile of the hydrophilic solid and the surface tension force dominates the bubble adhesion to hydrophilic surface in water.

2. Experimental

2.1. Sample preparation

Natural high-quality hematite and pyrite lumps were manually selected from Anshan ore mined in Liaoning Province, China. The hematite (Fe₂O₃) and pyrite (FeS₂) lumps were of 96+ wt.% and 99+ wt. % purity, respectively, as determined through x-ray fluorescence spectrometry (XRF) and x-ray diffraction (XRD). The XRD pattern shown in Fig. 1 was recorded with the X' Pert Pro multifunction diffractometer (Panalytical, Netherlands) using Cu K α radiation. The results of XRF analysis (ZSX Primus II, Rigaku, Japan) are shown in Table 1.

A diamond cut-off saw (SY<u>J</u>-40, MTI corporation, USA) was used to cut the hematite and pyrite lumps into smaller specimens having approximate dimensions of $10 \times 10 \times 5$ mm. Then, hematite and pyrite surfaces were polished using silicon carbide papers (Hudson Supply, USA) with mesh from #120 to #1200, followed by 6 μ m diamond and 1 μ m alumina powders (Allied High Tech Products, Inc., USA) as per

sequence listed in Table 2 to produce minerals of varying surface roughness. At each stage, the manual polishing of samples was carried out without tracking the time and directions of polishing, which resulted in hematite and pyrite surfaces having not identical roughness characteristics described by roughness parameters – defined in the following section.

2.2. Surface roughness measurement

The mineral surfaces were imaged under the MFP-3D Origin + atomic force microscope (Asylum Research, Oxford Instruments, USA) using the tapping mode and the ACT cantilevers (length $125\,\mu m,$ width $35\,\mu m,$ thickness $4.5\,\mu m)$ with a silicon tip (radius <10 nm, height 14--16 nm) obtained from Applied NanoStructures (Mountain View, CA, USA). At least three different locations were randomly selected for imaging $10\times10\,\mu m$ areas.

The root mean square (R_{RMS}) , average deviation (R_a) , surface area ratio (R_{SA}) , skewness (R_{sk}) , and kurtosis (R_{ku}) were analyzed and their average and standard deviation values are presented in this contribution. The R_{RMS} , R_a , R_{SA} , R_{sk} , and R_{ku} parameters are defined through the following equations:

$$R_{RMS} = \sqrt{\frac{1}{N} \sum_{i=1}^{N} Z_i^2} \tag{1}$$

$$R_{\alpha} = \frac{1}{N} \sum_{i=1}^{N} |Z_i - \overline{Z}| \tag{2}$$

$$R_{SA} = \frac{S_a}{S_p} \tag{3}$$

$$R_{sk} = \frac{1}{N} \sum_{i=1}^{N} \left(\frac{Z_i - \overline{Z}}{\sigma} \right)^3 \tag{4}$$

$$R_{ku} = \frac{1}{N} \sum_{i=1}^{N} \left(\frac{Z_i - \overline{Z}}{\sigma} \right)^4 - 3 \tag{5}$$

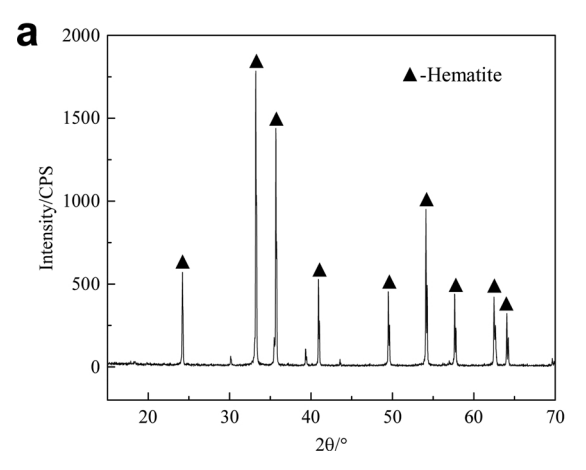
where $\sigma = \sqrt{\frac{1}{N-1}\sum_{i=1}^{N}(Z_i - \overline{Z})^2}$, Z_i is the height at a given pixel i, N is the total number of pixels in the image, and \overline{Z} is the average height of the entire image. S_a and S_p refer to the actual and projected surface area, respectively.

The correlations for experimental forces and contact angles versus surface roughness plotted and presented in further part of this contribution are limited to root mean square roughness (R_{RMS}) parameter because this parameter is more sensitive to large deviations such as occasional highs and lows as compared to R_a and R_{SA} values [48]. Both skewness and kurtosis are only used to describe normality of surface roughness

2.3. Measurement of adhesion force and contact angle

A high-sensitivity microelectronic mechanical balance (DCAT 21, Dataphysics, Germany), equipped with a charge-coupled device (CCD) camera was used in measurements of adhesion forces between air bubbles and sample surfaces, and recording the bubble-mineral interaction events [49–53]. Fig. 2 shows the schematic of the system (a), example of recorded force curve (b), and recorded images of air bubble during attachment and adhesion (c). All of the experimental values are the average of at least five independent measurements.

A mineral sample was placed in a transparent rectangular cell which was filled with deionized (DI) water. A $\sim 3\,\mu L$ volume air bubble was then produced using a pipette and placed in a platinum/iridium ring with the internal and external diameter of 2.06 and 2.42 mm, respectively, connected to the microbalance. The net force of this balance system was zeroed before force measurements. In this study, the mineral sample was raised up under a given velocity of 0.03 mm/s toward the air bubble, and then the velocity was reduced to 0.01 mm/s when



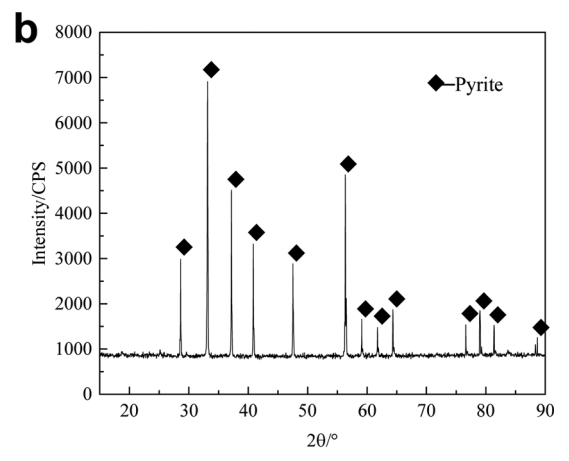


Fig. 1. XRD pattern for hematite (a) and pyrite (b).

Table 1
Multi-element chemical analyses of mineral sample (wt. %).

Samples	Total Fe	S	SiO_2	Al_2O_3	MgO	CaO	P
Hematite	68.9	0.04	1.78	0.24	0.03	0.08	0.03
Pyrite	46.2	52.9	0.73	0.02	0.01	0.02	0.03

Table 2
Polishing steps used in this study.

Sample Code	Polishing steps							
	Sandpap	Sandpaper (mesh)						
	120	400	1200		6 μm	1 μm		
S	+	+	+	+		+		
R1	+	+	+	+		-		
R2	+	+	+	-		-		
R3	+	+	-	-		-		
R4	+	-	-	-		-		

the sample surface contacted the air bubble. The sample moved upward to the compression distance (0.1 mm) pre-given by the system, after which, the sample was retracted at a constant velocity of 0.01 mm/s until a detachment of the air bubble from the sample surface.

The interactive force with respect to the surface position was recorded automatically. Fig. 2b shows the example of force curve. The force curve starts at the zero-background level. A sensitivity of the microbalance to vibrations causes the force curve to departure from a straight line. Because of a continuing submersion of air bubble into water, a small negative force caused by hydrostatic pressure is typically recorded before the bubble attaches to the mineral surface. Attachment and then spontaneous spreading of the air bubble results in measurement of the spreading force (SF). Passing the SF point in Fig. 2b, the mineral sample is pressed against the bubble to mechanically enlarge the bubble-mineral contact area over the predefined distance. As the next step, the sample is retreated from the compression end point causing the bubble to stretch until the maximum point at which maximum adhesion force is measured (MAF). Continuation of stretching leads to a decrease in bubble base diameter and spontaneous detachment of bubble from the mineral surface at point POF (pull-off force point). Concurrently with force measurements, the individual frames are captured by a CCD camera with the frame rate of 7.2 fps from which the contact angle (θ) and base diameter (2r) are measured (Fig. 2c). Examples of images of air bubbles at their multiple stages of approach, attachment, adhesion, and detachment to the magnesite mineral having varying nano-rough surface characteristics were provided in our earlier

publication [54].

3. Results

3.1. Surface roughness

The examples of 3D morphologies of hematite and pyrite surfaces are shown in Fig. 3. Table 3 summarizes the average and standard deviation values for roughness parameters determined in this study for both minerals polished according to the similar protocols. As expected, the surface roughness of minerals decreased at each step of polishing.

To prepare nearly smooth mineral surfaces, fine polishing with powder (after coarse polishing) was required. The final root-mean-square roughness of minerals varied between about $R_{RMS}=3$ and 4 nm ($R_a=2$ –3 nm, $R_{SA}\approx1$) (Table 3). By eliminating the final fine polishing, the R_{RMS} , R_a , and R_{SA} values increased to about 50 nm, 39 nm, and 1.017, respectively, for hematite and to about 18 nm, 14 nm, and 1.002, respectively, for pyrite. These roughness parameters increased to 246 nm, 193 nm, and 1.093 for hematite, and 255 nm, 178 nm, and 1.178 for pyrite, when the coarsest polishing was carried out alone (Table 3).

Low values for skewness (R_{sk}) and kurtosis (R_{ku}) in Table 3 suggest that the polishing produced symmetrical rough surfaces at almost every step of polishing. The R_{sk} values are very close to zero (with exception of pyrite S), suggesting that spatial distribution of asperity variations is symmetrical and follows a normal distribution. Low and positive values for R_{ku} indicate on uniformity of asperity variation. Larger values of R_{sk} and R_{ku} for pyrite S indicate the less symmetrical spatial distribution of nano-scaled asperities caused by non-uniform scratches that are produced by silicon carbide papers and left on the surface after the final fine polishing.

3.2. Force and contact angle measurements

Fig. 4 shows the adhesion forces, contact angles, and bubble base diameters of air bubbles measured on hematite and pyrite surfaces plotted with respect to R_{RMS} . The changes measured at the spreading point, maximum adhesion point, and pull-off point are discussed in the following subsection separately.

3.2.1. Spreading forces and receding contact angles

The (bubble) spreading force (F_s) was only detected on the smoothest surface where R_{RMS} is 3 nm for hematite and 4 nm for pyrite. As shown in Fig. 4a and b, the spreading force was only 12 μ N for hematite and 8 μ N for pyrite. The forces were too weak to be detected by the microbalance when the values of surface roughness were above 20 nm. This is because roughness of hydrophilic minerals induces a

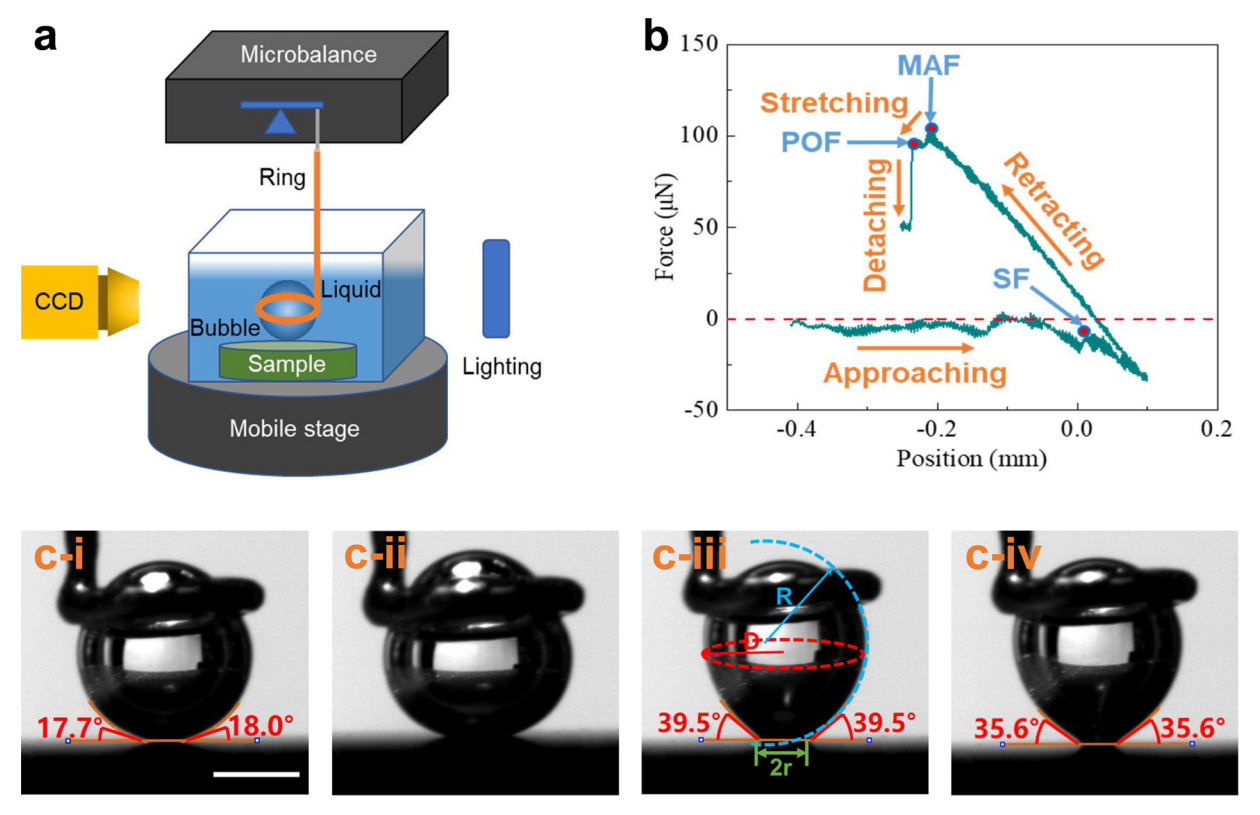


Fig. 2. (a) Schematic of the adhesion force measurement method for air bubble. **(b)** The typical force-distance curve recorded for the air bubble on the hematite surface, symbols include: SF - spreading force, MAF - maximum adhesion force, and POF - pull-off force. **(c)** Images of air bubble in contact with hematite surfaces $(R_{RMS} = 93 \text{ nm})$ at spreading point (c-i), compression end point (c-ii), maximum adhesion point (c-iii), and pull-off point (c-iv). The scale bar is 1.00 mm.

wider spreading of water on their surfaces [55] that prevents air bubble from attachment over larger contact areas; during the attachment process, the air bubble attempts to replace a water that covers the mineral. The contact angle measured for water after bubble attachment refers to the receding contact angle (θ_R), since the bubble forces the water to recede and open mineral area for attachment [50].

Fig. 4c and d show that the receding contact angles measured at the spreading point as a function of R_{RMS} . They are about 32° and 30° for hematite ($R_{RMS}=3$ nm) and pyrite ($R_{RMS}=4$ nm), respectively. θ_R systematically decreases to 17° and 20° for hematite and pyrite when the R_{RMS} of hematite and pyrite increases to about 50 nm and 18 nm, respectively. As shown in Fig. 4e and f, the bubble base diameter (2 r) decreases from about 0.52 to 0.27 mm for hematite and from 0.54 to 0.26 mm for pyrite when surfaces become rougher.

3.2.2. Maximum adhesion forces and most stable contact angles

As shown in Fig. 4a and b, in contrast to the spreading force (F_s), the maximum adhesion force (F_{max}) decreases more profoundly with the increasing roughness, from about 170 to 51 µN for hematite and from 174 to 38 µN for pyrite. The contact angle associated with the point of maximum adhesion force is called the most stable contact angle (θ_{max}) (the contact angle associated with the most stable water droplet/solid surface configuration and the state of lowest Gibbs energy for a system [56]). The θ_{max} value decreases from 66° to 27° for hematite and from 58° to 20° for pyrite (Fig. 4c and d) with increasing nano-scaled surface roughness. Similarly, the corresponding bubble base diameter decreases from 0.92 to 0.34 mm for hematite and from 0.90 to 0.29 mm for pyrite (Fig. 4e and f), indicating increasing resistance to advancement of the three-phase contact line that affects both the contact angle and adhesion force.

3.2.3. Pull-off forces and advancing contact angles

The adhesive strength at separation (pull-off) point decreases with

increasing R_{RMS} for both hematite and pyrite (Fig. 4a and b). Specifically, with the increasing of R_{RMS} from 3-4 to 250-260 nm, the pull-off force (F_{off}) decreases from 154 to 50 μ N for hematite and from 150 to 36 μ N for pyrite, having trends similar to those recorded for F_{max} (Fig. 4 and b) in previous subsection.

The water contact angle value measured at the point of pull-off force refers to the advancing contact angle (θ_A) [50]. The θ_A value decreases from 64° to 25° for hematite and from 56° to 19° for pyrite when the R_{RMS} roughness increases from 3–4 to 250–260 nm (Fig. 4c and d). The corresponding bubble base diameter decreases from 0.66 to 0.32 mm for hematite and 0.75 to 0.25 mm for pyrite (Fig. 4e and f).

4. Discussion

4.1. Bubble-hydrophilic surface adhesion forces

The submicroscopic mineral surface roughness with the R_{RMS} value less than 250 – 260 nm reduces the adhesive attachment with air bubble in water (Fig. 4). This is the result of increasing penetration of the rough surfaces of hydrophilic hematite and pyrite by water that can be explained qualitatively by the Wenzel model [57]:

$$\cos\theta_{w} = r_{w}\cos\theta_{s} \tag{6}$$

where θ_w is the contact angle on a rough solid surface, θ_S is the contact angle measured on the smooth surface of the same solid, and r_w refers to the roughness factor defined by the ratio of the actual surface area to its projection. However, in modern literature the roughness factor represents changes in the contact line on a rough surface compared to the changes in the contact line on a smooth and flat surface [58] (failure of original Wenzel model will be demonstrated in this contribution later).

The Wenzel equation or its modern modification clearly shows that the water contact angle decreases with increasing roughness factor (r_w) for any hydrophilic solid. In reverse systems as studied here, it means

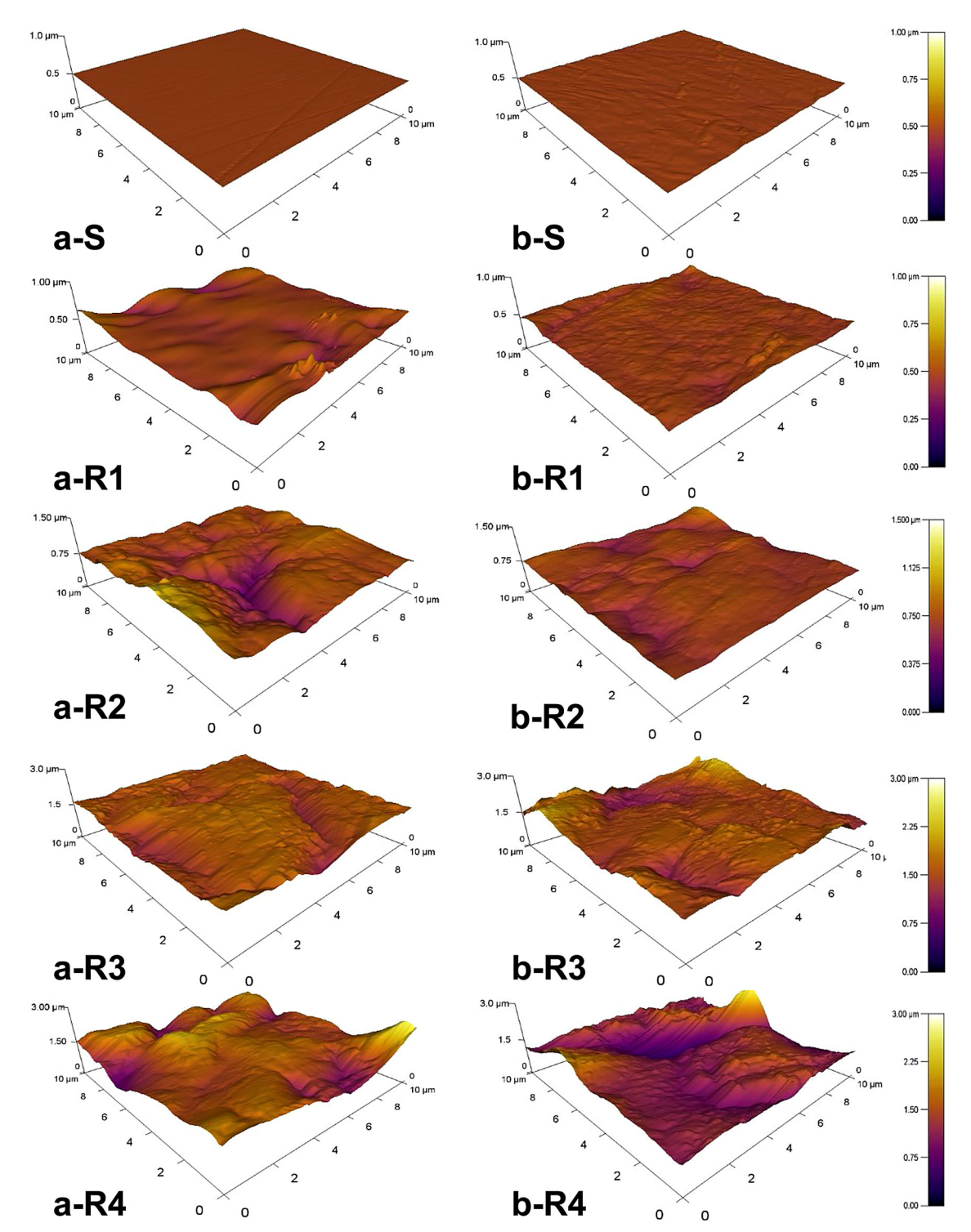


Fig. 3. AFM 3D-images of hematite (a) and pyrite (b) surfaces with different roughness (R_{RMS}).

that the air bubble faces increasing resistance from water to be removed from a rough surface when roughness features are significantly smaller than the area of bubble attachment contact [35].

The spreading, maximum adhesion, and pull-off forces for both hematite and pyrite are replotted on the same graphs in Fig. 5. The spreading force values were too small to clearly differentiate them from a noise on force curves recorded by the microbalance in this study and no clear correlation could be recorded. On a contrary, both maximum adhesion and pull-off forces reveal nearly a linear correlation with the $R_{RMS} < 260 \, \mathrm{nm}$.

The adhesion force between the droplet and a smooth solid surface, F, consists of two components (Eq. (7)). One is the vertical component of liquid-gas interfacial tension acting along the perimeter of triple contact line, known as surface tension force (F_T). The other is the Laplace pressure force (F_L), which is induced by the pressure difference across the liquid-gas interface for a stretched droplet. The combination of these two forces is expressed as [50,59,60]:

$$F = F_T - F_L = l\gamma \sin\theta - A\Delta P \tag{7}$$

where l is the length of the three-phase contact line which translates to

 Table 3

 The roughness parameters of mineral surfaces after the polishing treatment.

Mineral	Sample Code	R_{RMS} (nm)	R_a (nm)	R_{SA}	R_{sk}	R_{ku}
Hematite	S	3 ± 1	2 ± 1	1.000 ± 0.000	-0.61 ± 0.09	0.3 ± 0.6
	R1	50 ± 10	39 ± 8	1.017 ± 0.009	-0.5 ± 0.4	1.3 ± 0.7
	R2	93 ± 16	69 ± 12	1.025 ± 0.007	-0.4 ± 0.1	1.1 ± 0.5
	R3	127 ± 18	97 ± 15	1.059 ± 0.008	-0.48 ± 0.09	1.0 ± 1.1
	R4	246 ± 7	193 ± 8	1.093 ± 0.003	-0.15 ± 0.02	0.75 ± 0.07
Pyrite	S	4 ± 1	3 ± 1	1.000 ± 0.000	1.6 ± 2.2	3.0 ± 1.8
	R1	18 ± 3	14 ± 2	1.002 ± 0.001	-0.4 ± 0.1	0.4 ± 0.1
	R2	56 ± 8	42 ± 9	1.029 ± 0.013	-0.6 ± 0.4	1.7 ± 0.4
	R3	180 ± 12	127 ± 18	1.093 ± 0.012	0.0 ± 0.1	1.3 ± 0.7
	R4	255 ± 20	178 ± 20	1.178 ± 0.018	-0.2 ± 0.3	1.2 ± 1.1

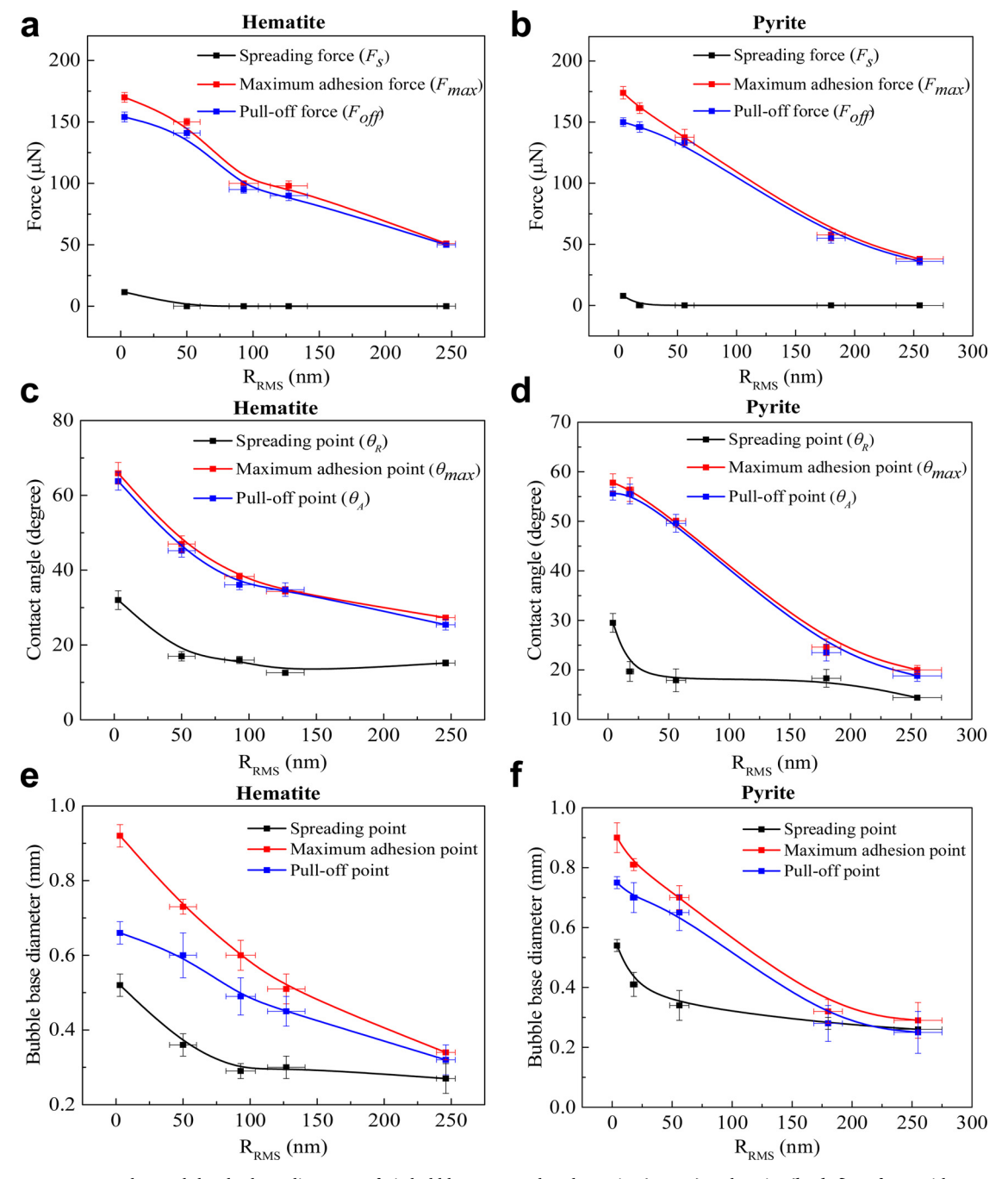


Fig. 4. Forces, contact angles, and droplet base diameters of air bubbles measured on hematite (a, c, e) and pyrite (b, d, f) surfaces with respect to R_{RMS} .

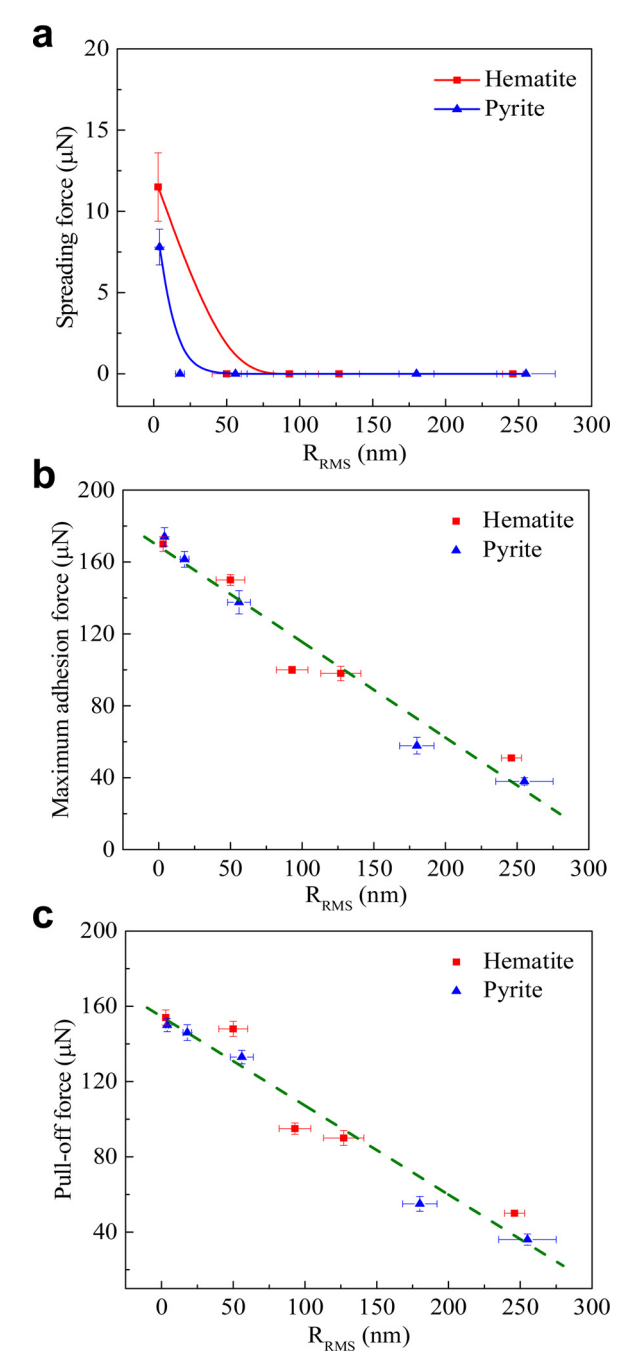


Fig. 5. Spreading force (F_s) (a), maximum adhesion force (F_{max}) (b), and pull-off force (F_{off}) (c) of an air bubble measured on hematite and pyrite surfaces with respect to R_{RMS} . The lines in (b) and (c) represent linear fitting line.

the perimeter of bubble base ($l=2\pi r$ for a circular base on a smooth solid surface; r is the radius of bubble base that is in contact with the substrate), γ is the liquid-gas interfacial tension, θ is the contact angle, A is the projected contact area for the bubble base ($A=\pi r^2$), and ΔP is the Laplace pressure defined as:

$$\Delta P = \gamma \left(\frac{1}{D} + \frac{1}{R}\right) \tag{8}$$

where D and R are the principal radii of the air bubble (Fig. 2c).

In case of an air bubble on a rough surface, Eq. (7) is modified to include the actual length of contact line ($2\pi rx$, where x is a normalized contact line; defined as the actual droplet contact line along the bubble perimeter normalized by the apparent bubble perimeter) [53]:

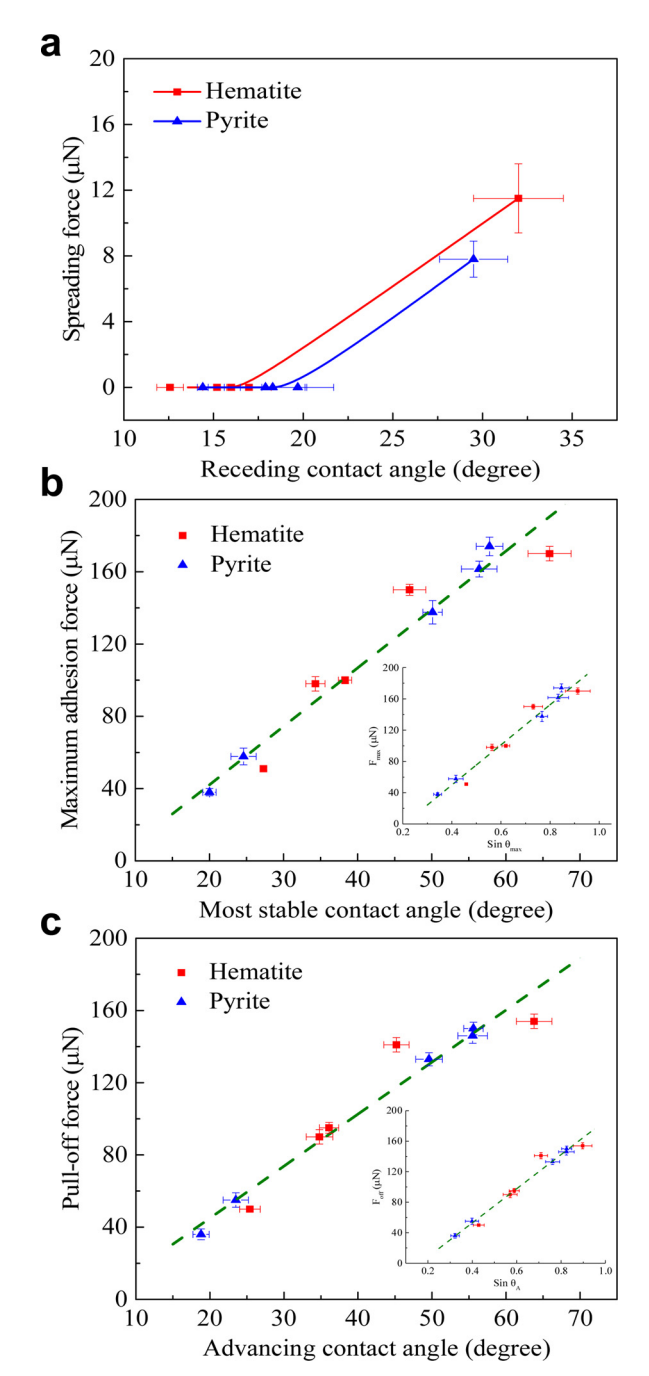


Fig. 6. Spreading force (F_s) (a), maximum adhesion force (F_{max}) (b), and pull-off force (F_{off}) (c) of an air bubble measured on the hematite and pyrite surfaces, with respect to contact angles. The inserts in (b) and (c) show the correlation between the adhesion force with respect to sine of contact angle. The lines in (b) and (c) represent the linear fitting line.

$$F = F_T - F_L = 2\pi r x \gamma \sin\theta - \pi r^2 \Delta P \tag{9}$$

Eq. (9) suggests that the adhesion force of an air bubble is also dependent on the contact angle, which is also affected by roughness as discussed earlier. Thus, the spreading, maximum adhesion, and pull-off forces were replotted with respect to the receding, most stable, and advancing contact angles, respectively, as shown in Fig. 6.

There is no clear correlation between the spreading force and receding contact angle because the spreading force values were too small to separate them from the baseline and noise when the contact angles were below 20° for both hematite and pyrite (Fig. 6a). On a contrary, maximum adhesion and pull-off forces increase nearly linearly with the

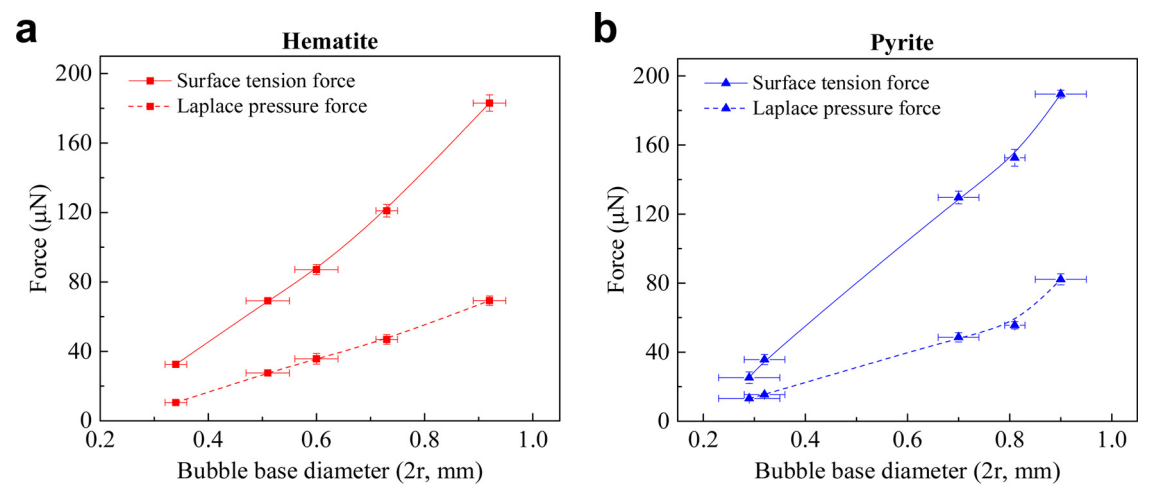


Fig. 7. Surface tension force and Laplace pressure force for the bubbles measured on the hematite (a) and pyrite (b) surfaces with varying roughness, with respect to the bubble base diameters.

increasing most stable and advancing contact angles (and their sine function), respectively, for both hematite and pyrite (Fig. 6b and c). These results confirm the importance of contact angle in analysis of adhesion forces and suggest that the surface tension force dominates the adhesion between air bubble and nano-scaled surface of hydrophilic rough solid.

Both the surface tension force $(F_T = 2\pi r \gamma \sin \theta)$ and Laplace pressure fore $(F_L = \pi r^2 \Delta P)$ were calculated based on experimentally measured r, ΔP , and θ values for bubble shapes at points of maximum adhesion force and are shown in Fig. 7. For both minerals, the surface tension force is significantly larger than the Laplace pressure force and the difference increases with the increasing R_{RMS} , suggesting the F_T is the dominant contributor to the maximum adhesion force.

As shown in Fig. 4 and discussed earlier, the results demonstrate that the submicroscopic roughness significantly reduces adhesive strength of an air bubble with mineral surface, especially the maximum adhesion force that dropped from 170 to 51 μN for hematite and from 174 to 38 μN for pyrite. The following sections provide further analysis based on the above results to reveal the role of the surface roughness in the adhesion strength.

4.2. Roughness factor: AFM versus Wenzel equation

As discussed earlier, the Wenzel Eq. (6) predicts the cosine of a contact angle on the rough surface as a function of roughness factor. In this study, the Wenzel equation was used to calculate the roughness factor based on experimental most stable contact angle values and assumption that the contact angle measured for the surfaces with $R_{RMS} = 3$ and 4 nm represents water contact angle on a smooth mineral surface. It is rather crude assumption, as will be concluded later, but necessary if the equilibrium contact angle for the atomically smooth surface remains unknown.

Fig. 8a and b show the roughness factor (r_w) calculated by the Wenzel Eq. (6) as a function of R_{RMS} and R_{SA} , respectively, both measured with AFM. Note that r_w can refer here to either ratio of surface areas or contact line lengths (see Section 4.1). For both minerals, the r_w increases with the increase in R_{RMS} (Fig. 8a). Specifically, r_w increases from 1.0–2.2 and 1.8 for hematite and pyrite, respectively; calculated r_w of hematite is higher than that of pyrite at the given R_{RMS} . Calculated r_w of hematite is higher than that of pyrite at the given R_{RMS} . This is indicative of more complex local contortions of the three-phase contact line (bubble base perimeter) [39]; the line departures from a circular shape characteristic to the bubble base on a perfectly smooth surface.

Fig. 8b suggests that the r_w values for hematite and pyrite with different R_{RMS} are much higher than R_{SA} measured by AFM. This

significant difference in r_w and R_{SA} values originates from three sources. First, as mentioned in Section 4.1, the r_w value in the modified (and correct) Wenzel equation represents the ratio of the actual contact line length to its projection. Therefore, the equation as originally proposed by Wenzel in 1936 [57], which takes into account the ratio of the actual contact area to its projection (as per definition of R_{SA}) does not apply here. Unfortunately, experimental verification of the r_w value based on actual and projected contact line lengths on nano-rough surfaces is beyond experimental capability of our laboratory. Second, Eq. (6) was theoretically derived based on assumption that contortion of the contact line follows a profile of a rough surface in a vertical direction. In practice, the roughness also causes a lateral contortion of the contact line that theoretical Eq. (6) does not account for. Finally, the R_{SA} values determined through AFM roughness analysis are typically underestimated because the cantilever tip cannot image surface features that are smaller than the tip dimension and due to a tip deconvolution effect [46,61].

4.3. Contortion of the contact line

The contortion of the contact line at the point of maximum adhesion force can be represented by the x values (Eq. (9)). The x value was calculated using experimental values of F, r, θ , and ΔP and using the following equation:

$$x = \frac{F + \pi r^2 \Delta P}{2\pi r \gamma sin\theta} \tag{10}$$

The x value represents the ratio between actual (on a rough surface) and apparent (on a smooth surface) contact line (perimeter of the bubble base), which accounts for both vertical and lateral contortions of the line. We compare this value with r_w value (Eq. (6)) that also defines the ratio between actual and apparent contact line but considers only vertical contortion of the contact line – as discussed in the previous section.

Fig. 9a and b plot the average calculated x values as a function of R_{RMS} and r_w for both hematite and pyrite. The x value increases from about 1.4 to 2.1 with the increase in R_{RMS} suggesting the contortion of the contact line increases with increasing R_{RMS} . For both minerals, hematite and pyrite, the x values are basically identical at the given R_{RMS} , and follow a nearly linear correlation. At a first glance, the value of x=1.4 for "smooth" minerals appears too large as it should be equal to 1 for atomically smooth surfaces. Unfortunately, both hematite and pyrite had residual roughness at a level of 3-4 nm after the final polishing. Additionally, and surprisingly, the most recent imaging of ionic liquids on atomically smooth surface of mica and nearly atomically

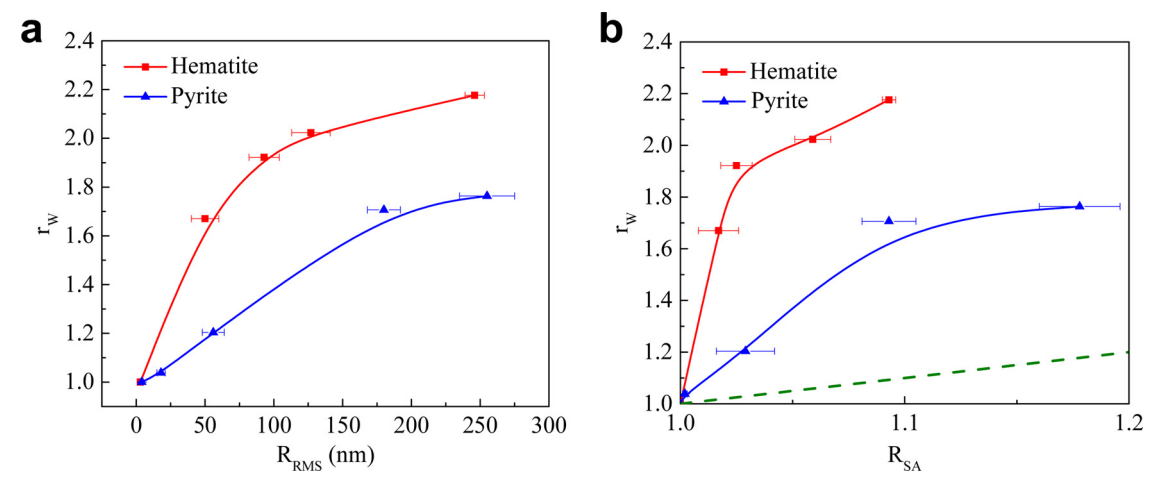


Fig. 8. Roughness ratio (r_w) calculated by Wenzel equation with respect to R_{RMS} (a) and R_{SA} (b) measured by AFM for hematite and pyrite. The dashed line in (b) is plotted by equation of y = x.

smooth silicon wafer using a high-resolution helium ion microscopy revealed nano-scale waving and wrinkling of the contact line [62]. This new experimental revelation, if correct, could change our analysis of the three-phase contact line.

Fig. 9b shows a correlation between calculated x and r_w values. The data are significantly scattered, but they cluster around a linear relationship. Deviations from linearity could originate from the limited accuracy in measurements of contact angle, bubble base diameter, and the principal radii of the stretched bubble determined via the captured images. In view of comment in the previous paragraph, it could also originate from a false assumption that there was no contortion of the contact line on the smoothest surfaces of hematite and pyrite.

The linear match (dashed line) between x and r_w values would indicate a consistent vertical contortion of the contact line. Indeed, for hematite with nano-scaled roughness, the r_w values are close to x values. On the other hand, the x values for pyrite are consistently higher than r_w values indicating that lateral contortion of the bubble base perimeter was more developed on pyrite than hematite.

4.4. Broader implications of this study

Although only two hydrophilic natural minerals were selected and used in this study, the general correlations recorded and conclusions drawn should apply to all hydrophilic specimens of different surface chemistry that have similar both nano-roughness characteristics and

affinity to water in term of most stable contact angle ($\sim 10-70^{\circ}$). This study provides guidelines for engineering hydrophilic surfaces with nano-scale roughness characteristics needed for a control over adhesion of gas bubbles to such surfaces, and benefiting microfluidic and microanalytical systems design.

The measurements of adhesion forces for air bubbles were carried out in pure water and therefore, the results do not apply directly to flotation systems unless reagent-free flotation techniques are explored. In flotation of minerals, including pyrite and hematite, additional surface-active reagents such as collectors and frothers are necessary that reduce surface tension of water. Unfortunately, surface-active regents cannot be used in our experimental set-up because their addition would cause weakening of the ring holder-bubble interactions and causing premature detachment of bubble from the ring. Therefore, application of this microbalance to adhesion force measurements in aqueous solutions of surface-active reagents requires design of different bubble holder, which is beyond the scope of this contribution.

5. Conclusions

The spreading, maximum adhesion, and pull-off forces were measured for air bubbles in contact with hydrophilic hematite and pyrite surfaces immersed in water using a sensitive microbalance. Surfaces of minerals were engineered to have the range of nano-scaled (random) surface roughness defined by the root-mean-square (RMS) roughness

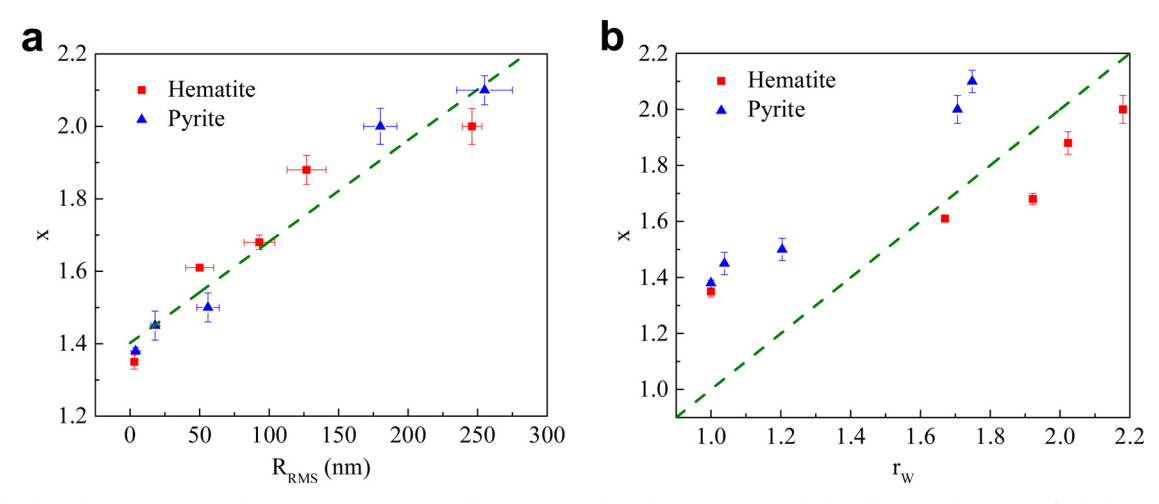


Fig. 9. Calculated roughness ratio (x) with respect to R_{RMS} measured by AFM (**a**) and roughness ratio (r_w) calculated by Wenzel equation (**b**) for hematite and pyrite. The line in (a) represents linear fitting line, and the line in (b) is plotted by equation of y = x.

between 3 and 260 nm. The following specific conclusions result from this research:

- 1) In qualitative agreement with the Wenzel model, increasing submicroscopic (random) roughness of both hydrophilic specimens enhances the strength of interactions with water making its displacement with air bubble more difficult. The bubble-mineral adhesion force decreased from about 170 to 40–50 μN when RMS increased from 3-4 to 250-260 nm. However, experimental data failed to predict the most stable contact angles on nano-scaled rough surface when using the original Wenzel equation.
- 2) The surface tension force is the dominant contributor to the maximum adhesion force between bubble and nano-scaled rough surface of hydrophilic minerals of hematite and pyrite.
- 3) A linear dependence between both maximum adhesion and pull-off forces and RMS values was found for both hydrophilic minerals, which could simplify any future designing of nano-scaled roughness of hydrophilic surfaces interacting with gas bubbles in water.
- 4) Also, a linear correlation between the maximum adhesion force and most stable contact angle (and its sines function) is reported, indicating that surface tension force dominates bubble adhesive interaction with nano-rough hydrophilic surfaces.
- 5) The results indicate that the AFM analysis of nano-scaled rough surfaces underestimates the true surface area and calculated roughness factor needed for the Wenzel model. For example, analysis of this factor based on experimental contact angle values and adhesion forces suggest this parameter to be between 1.4 and 2.2 for hydrophilic surfaces with RMS from 3 to 260 nm instead of 1.0–1.2 as AFM analysis indicates.

CRediT authorship contribution statement

Donghui Wang: Conceptualization, Investigation, Methodology, Writing - original draft. Zhanglei Zhu: Resources, Validation. Bin Yang: Methodology, Visualization. Wanzhong Yin: Supervision, Resources, Funding acquisition. Jaroslaw W. Drelich: Supervision, Validation, Writing - review & editing, Funding acquisition.

Declaration of Competing Interest

The authors declare that they have no known competing financial interests or personal relationships that could have appeared to influence the work reported in this paper.

Acknowledgements

The authors gratefully acknowledge the financial support provided by the National Natural Science Foundation of China (No. 51874072 and 51974064), and the Fundamental Research Funds for the Central Universities (No. N180106006 and N2001029). Donghui Wang (No. 201806080137) also appreciates China Scholarship Council for the financial support for his research study at Michigan Technological University, United States. Financial support for purchasing atomic force microscope used in characterization of mineral roughness through NSF-CS-MRI grant (No. 1725818) is appreciated as well.

References

- [1] B. Albijanic, O. Ozdemir, A.V. Nguyen, D. Bradshaw, A review of induction and attachment times of wetting thin films between air bubbles and particles and its relevance in the separation of particles by flotation, Adv. Colloid Interface Sci. 159 (2010) 1–21.
- [2] B. Yang, W. Yin, Z. Zhu, D. Wang, H. Han, Y. Fu, H. Sun, F. Chu, J. Yao, A new model for the degree of entrainment in froth flotation based on mineral particle characteristics, Powder Technol. 354 (2019) 358–368.
- [3] W. Yin, D. Wang, J.W. Drelich, B. Yang, D. Li, Z. Zhu, J. Yao, Reverse flotation separation of hematite from quartz assisted with magnetic seeding aggregation,

- Miner. Eng. 139 (2019) 105873.
- [4] M. Kemper, State-of-the-art and new technologies in flotation deinking, Int. J. Miner. Process. 56 (1999) 317–333.
- [5] S. Vashisth, C.P. Bennington, J.R. Grace, R.J. Kerekes, Column flotation deinking: state-of-the-art and opportunities, resources, Conserv. Recycl. 55 (2011) 1154–1177.
- [6] J. Drelich, T. Payne, J. Kim, J. Miller, R. Kobler, S. Christiansen, Selective froth flotation of PVC from PVC/PET mixtures for the plastics recycling industry, Polym. Eng. Sci. 38 (1998) 1378–1386.
- [7] C.-q. Wang, H. Wang, J.-g. Fu, Y.-n. Liu, Flotation separation of waste plastics for recycling—a review, Waste Manag. 41 (2015) 28–38.
- [8] J. Drelich, J. Kim, T. Payne, J. Miller, R. Kobler, Purification of polyethylene terephthalate from polyvinyl chloride by froth flotation for the plastics (soft-drink bottle) recycling industry, Sep. Purif. Technol. 15 (1999) 9–17.
- [9] J. Rubio, M. Souza, R. Smith, Overview of flotation as a wastewater treatment technique, Miner. Eng. 15 (2002) 139–155.
- [10] X. Cai, J. Chen, M. Liu, Y. Ji, S. An, Numerical studies on dynamic characteristics of oil-water separation in loop flotation column using a population balance model, Sep. Purif. Technol. 176 (2017) 134–144.
- [11] J. Masliyah, Z.J. Zhou, Z. Xu, J. Czarnecki, H. Hamza, Understanding water-based bitumen extraction from Athabasca oil sands, Can. J. Chem. Eng. 82 (2004) 628–654.
- [12] F. Rao, Q. Liu, Froth treatment in Athabasca oil sands bitumen recovery process: a review, Energy Fuels 27 (2013) 7199–7207.
- [13] F. Lin, L. He, J. Hou, J. Masliyah, Z. Xu, Role of ethyl cellulose in bitumen extraction from oil sands ores using an aqueous–nonaqueous hybrid process, Energy Fuels 30 (2016) 121–129.
- [14] J. Drelich, D. Leliński, J. Hupka, J.D. Miller, The role of gas bubbles in bitumen release during oil sand digestion, Fuel 74 (1995) 1150–1155.
- [15] Y. Xia, R. Zhang, Y. Xing, X. Gui, Improving the adsorption of oily collector on the surface of low-rank coal during flotation using a cationic surfactant: an experimental and molecular dynamics simulation study, Fuel 235 (2019) 687–695.
- [16] Y. Xing, X. Gui, Y. Cao, D. Wang, H. Zhang, Clean low-rank-coal purification technique combining cyclonic-static microbubble flotation column with collector emulsification, J. Clean. Prod. 153 (2017) 657–672.
- [17] E. Dickinson, Food emulsions and foams: stabilization by particles, Curr. Opin. Colloid Interface Sci. 15 (2010) 40–49.
- [18] P. Wierenga, H. Gruppen, New views on foams from protein solutions, Curr. Opin. Colloid Interface Sci. 15 (2010) 365–373.
- [19] G. Lomolino, S. Vincenzi, D. Gazzola, A. Crapisi, A. Curioni, Foaming properties of potato (Solanum tuberosum) proteins: a study by the gas sparging method, Colloids Surf. A Physicochem. Eng. Asp. 475 (2015) 75–83.
- [20] A.-L. Fameau, A. Saint-Jalmes, Non-aqueous foams: current understanding on the formation and stability mechanisms, Adv. Colloid Interface Sci. 247 (2017) 454–464.
- [21] N. Müller-Fischer, D. Suppiger, E.J. Windhab, Impact of static pressure and volumetric energy input on the microstructure of food foam whipped in a rotor–stator device, J. Food Eng. 80 (2007) 306–316.
- [22] A. Arzhavitina, H. Steckel, Foams for pharmaceutical and cosmetic application, Int. J. Pharm. 394 (2010) 1–17.
- [23] T.S. Horozov, Foams and foam films stabilised by solid particles, Curr. Opin. Colloid Interface Sci. 13 (2008) 134–140.
- [24] T. Bujak, T. Wasilewski, Z. Nizioł-Łukaszewska, Role of macromolecules in the safety of use of body wash cosmetics, Colloids Surf. B Biointerfaces 135 (2015) 497–503.
- [25] A. Bureiko, A. Trybala, N. Kovalchuk, V. Starov, Current applications of foams formed from mixed surfactant–polymer solutions, Adv. Colloid Interface Sci. 222 (2015) 670–677.
- [26] M. Prakash, N. Gershenfeld, Microfluidic bubble logic, Science 315 (2007) 832–835.
- [27] J.I. Park, Z. Nie, A. Kumachev, A.I. Abdelrahman, B.P. Binks, H.A. Stone, E. Kumacheva, A microfluidic approach to chemically driven assembly of colloidal particles at gas-liquid interfaces, Angew. Chemie Int. Ed. 48 (2009) 5300–5304.
- [28] D.D. Meng, Micropumping of liquid by directional growth and selective venting of gas bubbles, Lab Chip 8 (2008) 958–968.
- [29] J.D. Zahn, A.P. Pisano, D. Liepmann, Continuous on-chip micropumping for microneedle enhanced drug delivery, Biomed. Microdevices 6 (2004) 183–190.
- [30] E.D. Torniainen, A.N. Govyadinov, D.P. Markel, P.E. Kornilovitch, Bubble-driven inertial micropump, Phys. Fluids 24 (2012) 122003.
- [31] R.J. Lemmens, D.D. Meng, A comparative study on bubble-driven micropumping in microchannels with square and circular cross sections, Sens. Actuators A Phys. 169 (2011) 164–170.
- [32] V. Singhal, S.V. Garimella, A. Raman, Microscale pumping technologies for microchannel cooling systems, Appl. Mech. Rev. 57 (2004) 191–221.
- [33] C. Zhou, H. Zhang, Z. Li, W. Wang, Chemistry pumps: a review of chemically powered micropumps, Lab Chip 16 (2016) 1797–1811.
- [34] D. Patra, S. Sengupta, W. Duan, H. Zhang, R. Pavlick, A. Sen, Intelligent, self-powered, drug delivery systems, Nanoscale 5 (2013) 1273–1283.
- [35] J.W. Drelich, A. Marmur, Meaningful contact angles in flotation systems: critical analysis and recommendations, Surf. Innov. 6 (2017) 19–30.
- [36] Z. Li, F. Rao, M.A. Corona-Arroyo, A. Bedolla-Jacuinde, S. Song, Comminution effect on surface roughness and flotation behavior of malachite particles, Miner. Eng. 132 (2019) 1–7.
- [37] W. Xia, Role of surface roughness in the attachment time between air bubble and flat ultra-low-ash coal surface, Int. J. Miner. Process. 168 (2017) 19–24.
- [38] R.A. Pushkarova, R.G. Horn, Bubble solid interactions in water and electrolyte

- solutions, Langmuir 24 (2008) 8726-8734.
- [39] J.W. Drelich, Contact angles: from past mistakes to new developments through liquid-solid adhesion measurements, Adv. Colloid Interface Sci. 267 (2019) 1–14.
- [40] J.W. Drelich, L. Boinovich, E. Chibowski, C. Della Volpe, L. Hołysz, A. Marmur, S. Siboni, Contact angles: history of over 200 years of open questions, Surf. Innov. 8 (2020) 3–27.
- [41] M. Krasowska, K. Malysa, D.A. Beattie, Recent advances in studies of bubble-solid interactions and wetting film stability, Curr. Opin. Colloid Interface Sci. 44 (2019) 48–58.
- [42] Y. Xing, X. Gui, L. Pan, B.-E. Pinchasik, Y. Cao, J. Liu, M. Kappl, H.-J. Butt, Recent experimental advances for understanding bubble-particle attachment in flotation, Adv. Colloid Interface Sci. 246 (2017) 105–132.
- [43] L. Xie, C. Shi, X. Cui, J. Huang, J. Wang, Q. Liu, H. Zeng, Probing the interaction mechanism between air bubbles and bitumen surfaces in aqueous media using bubble probe atomic force microscopy, Langmuir 34 (2018) 729–738.
- [44] Z. Gao, R. Fan, J. Ralston, W. Sun, Y. Hu, Surface broken bonds: an efficient way to assess the surface behaviour of fluorite, Miner. Eng. 130 (2019) 15–23.
- [45] O. Guven, M.S. Celik, J.W. Drelich, Flotation of methylated roughened glass particles and analysis of particle-bubble energy barrier, Miner. Eng. 79 (2015)
- [46] Z. Zhu, D. Wang, B. Yang, W. Yin, M.S. Ardakani, J. Yao, J.W. Drelich, Effect of nano-sized roughness on the flotation of magnesite particles and particle-bubble interactions, Miner. Eng. 151 (2020) 106340.
- [47] J.W. Drelich, A simplified analysis of the effect of nano-asperities on particle-bubble interactions, Physicochem. Prob. Min. Process. 54 (2018) 10–18.
- [48] E. Gadelmawla, M. Koura, T. Maksoud, I. Elewa, H. Soliman, Roughness parameters, J. Mater. Process. Technol. 123 (2002) 133–145.
- [49] Y. Jiang, Y. Sun, J.W. Drelich, C.-H. Choi, Spontaneous spreading of a droplet: the role of solid continuity and advancing contact angle, Langmuir 34 (2018) 4945–4951
- [50] Y. Sun, Y. Jiang, C.-H. Choi, G. Xie, Q. Liu, J.W. Drelich, Direct measurements of adhesion forces of water droplets on smooth and patterned polymers, Surf. Innov. 6

- (2018) 93-105.
- [51] Y. Sun, Y. Jiang, C.-H. Choi, G. Xie, Q. Liu, J.W. Drelich, The most stable state of a droplet on anisotropic patterns: support for a missing link, Surf. Innov. 6 (2018) 133–140.
- [52] Y. Sun, Y. Li, X. Dong, X. Bu, J.W. Drelich, Spreading and adhesion forces for water droplets on methylated glass surfaces, Colloids Surf. A Physicochem. Eng. Asp. 591 (2020) 124562.
- [53] D. Wang, Y. Jiang, Z. Zhu, W. Yin, K. Asawa, C.-H. Choi, J.W. Drelich, Contact line and adhesion force of droplets on concentric ring-textured hydrophobic surfaces, Langmuir 36 (2020) 2622–2628.
- [54] Z. Zhu, D. Wang, B. Yang, W. Yin, J.W. Drelich, Water droplets and air bubbles at magnesite nano-rough surfaces: analysis of induction time, adhesion and detachment using a dynamic microbalance, Miner. Eng. 155 (2020) 106449.
- [55] J. Drelich, E. Chibowski, Superhydrophilic and superwetting surfaces: definition and mechanisms of control, Langmuir 26 (2010) 18621–18623.
- [56] A. Marmur, C. Della Volpe, S. Siboni, A. Amirfazli, J.W. Drelich, Contact angles and wettability: towards common and accurate terminology, Surf. Innov. 5 (2017) 3–8.
- [57] R.N. Wenzel, Resistance of solid surfaces to wetting by water, Ind. Eng. Chem. 28 (1936) 988–994.
- [58] L. Gao, T.J. McCarthy, How Wenzel and Cassie were wrong, Langmuir 23 (2007) 3762–3765.
- [59] J. Qian, H. Gao, Scaling effects of wet adhesion in biological attachment systems, Acta Biomater. 2 (2006) 51–58.
- [60] H. Chen, T. Tang, H. Zhao, K.-Y. Law, A. Amirfazli, How pinning and contact angle hysteresis govern quasi-static liquid drop transfer, Soft Matter 12 (2016) 1998–2008.
- [61] Z. Zhu, W. Yin, H. Han, S. Cao, B. Yang, D. Wang, Investigation on the influence of surface roughness on magnetite flotation from the view of both particle-particle and bubble-particle interactions, Colloids Surf. A Physicochem. Eng. Asp. (2020) 124681.
- [62] Q. Liu, J. Yu, H. Wang, The role of the substrate roughness in contact angle hysteresis and dynamic deviation, Int. J. Heat Mass Transf. 148 (2020) 118985.